January and July Simulations with a Spectral General Circulation Model

ERIC J. PITCHER

Rosenstiel School of Marine and Atmospheric Science, University of Miami, Miami, FL 33149

ROBERT C. MALONE

Institute for Geophysics and Planetary Physics, Los Alamos National Laboratory, Los Alamos, NM 87545

V. RAMANATHAN AND MAURICE L. BLACKMON

National Center for Atmospheric Research,[1] Boulder, CO 80307

KAMAL PURI AND WILLIAM BOURKE

Australian Numerical Meteorology Research Centre, Melbourne, Australia 3001

(Manuscript received 25 May 1982, in final form 26 August 1982)

ABSTRACT

We describe the results of January and July simulations carried out with a nine-level spectral model, employing a rhomboidal truncation at wavenumber 15. Sea-surface temperature, sea-ice distribution and solar zenith angle are held constant in each simulation. The model includes interactive clouds and radiative processes after Ramanathan *et al.* (1983). Selected fields are shown which highlight the model's strengths and weaknesses.

The latitude–height distribution of the zonal wind is successfully simulated. The model captures the separation between the wintertime westerly jets in the troposphere and stratosphere and thus simulates the sign reversal in the vertical wind shear across the jet axis in the upper troposphere.

In addition to the zonal wind, we show also the zonally averaged temperature, meridional wind and vertical velocity. Regional distributions of sea-level pressure, surface air temperature, precipitation and a number of other fields defined at various pressure levels are compared in detail with observations. For the most part, the large-scale features of the observed general circulation are successfully simulated, although the sea-level pressure in the subtropics over continental regions in the wintertime is higher than observed, and the model atmosphere tends to be a few degrees colder than observed. We offer a partial explanation for this last deficiency.

There is good agreement between the model stratosphere and the actual stratosphere. Preliminary indications suggest the variability present in the model is comparable to that found in the atmosphere.

1. Introduction

Spectral models have recently emerged as an attractive alternative to finite-difference models in simulating the general circulation of the atmosphere (Bourke *et al.*, 1977; Manabe *et al.*, 1979). That this is so derives principally from the inherent advantages of the spectral method with respect to elimination of aliasing, accuracy of derivative evaluation and ease of global modeling. From a practical standpoint, these advantages have only been fully realized through the advent of transform methods (Eliasen *et al.*, 1970; Orszag, 1970), which permit the efficient computation of nonlinear terms in the equations of motion, and facilitate the local incorporation of "physical" processes in three-dimensional space. Furthermore, and perhaps of equal importance, the time marching within a spectral model may be handled via a semi-implicit technique (Robert, 1969) with relative ease. Consequently, for roughly comparable resolution, a spectral model is more economical of computer time than a finite-difference model employing an explicit scheme for time integration.

Using the spectral model of Bourke *et al.* (1977), McAvaney *et al.* (1978) carried out a global simulation of the January climate, demonstrating the viability of the spectral technique for general circulation studies. This model has recently undergone a number of changes. The most significant of these has been the incorporation of a cloud/radiation formulation described in detail by Ramanathan *et al.* (1983). In addition, the model has been reprogrammed to exploit the architecture of the CRAY-1 computer, and, with a rhomboidal truncation at wavenumber 15, less than

[1] The National Center for Atmospheric Research is sponsored by the National Science Foundation.

2 min is required to advance the model atmosphere by one day.

With the installation of the new prescription for the evaluation of radiative transfer, the performance of the model improved, the most notable improvement being a more realistic simulation of the zonal-wind profile. The model now predicts a separation between the wintertime westerly jets in the troposphere and stratosphere, and the zonal-wind speeds in the model stratosphere are in accord with observations.

In the light of these and other improvements, we present in this paper a description of the model's current performance. We do not intend for this study to be an exhaustive documentation of the model's performance, but, instead, we wish to show selected fields, chosen to highlight the model's strengths and weaknesses. The results given in this paper could serve as a benchmark against which climate-sensitivity experiments carried out with this model might be compared. Likewise, the effects of future model improvements could be assessed by comparison with the simulated fields given here.

January and July represent the most extreme climates for which sufficiently detailed observational data are available. In this paper we describe the results of simulations in which the model was run in both perpetual January and July modes. Extended integrations were carried out with the model (in some cases up to 1200 days) ensuring that the results are representative of an equilibrium state, completely free of the influence of the initial conditions. These data are now available for examination by interested scientists.

After providing a brief description of the model[2] in Section 2, we show a number of zonally averaged variables in Section 3. Section 4 assesses the model's ability to simulate the geographical variations that are so readily apparent in meteorological fields. An indication of the temporal variability found in the model is given in Section 5.

2. Model summary

A detailed description of the model's formulation may be found in Bourke (1974) and Bourke *et al.* (1977) with many of the essential features summarized in McAvaney *et al.* (1978). The current version of the model differs from the one described in these earlier papers principally in the treatment of radiative processes.

a. Basic features

The vertical coordinate $\sigma = p/p_*$ (p_* is the surface pressure) is adopted from Phillips (1957), and the equations of motion are derived in this system. The model levels, at which σ assumes the values of 0.991, 0.926, 0.811, 0.664, 0.500, 0.336, 0.189, 0.074 and 0.009, are identical to those chosen by McAvaney *et al.* (1978) and to those used in many GFDL model simulations. The vertical component of relative vorticity and the divergence of the horizontal wind serve as the prognostic variables for the horizontal motion field. The continuity equation is recast as a prognostic equation for the logarithm of surface pressure. Predictive equations for temperature and water vapor mixing ratio complete the system of prognostic equations. We take $\dot{\sigma} = d\sigma/dt = 0$ at $\sigma = 0$ and $\sigma = 1$.

At each discrete vertical level the dependent variables are expanded in a truncated series of spherical harmonics, e.g. for temperature T we have

$$T(\lambda, \phi, \sigma, t) = \sum_{m=-J}^{+J} \sum_{l=|m|}^{|m|+J} T_l^m(\sigma, t) Y_l^m(\lambda, \phi),$$

where T_l^m denotes a time-dependent expansion coefficient, Y_l^m a spherical harmonic, spatially dependent on latitude ϕ and longitude λ, and J the rhomboidal wavenumber truncation (Ellsaesser, 1966). The number of waves around a latitude circle is given by $|m|$ while $l-|m|$ denotes the number of zero crossings between the poles. The model dynamics employ a spectral-to-grid transform, including a vectorized fast Fourier transform designed for use on the CRAY-1 computer. There are 40 Gaussian latitudes between poles with spacing of $\sim 4.4°$ and 48 equally spaced longitude points. The model is advanced in time by a semi-implicit time integration with a timestep of 30 minutes.

Included in the model are the following parameterized physical processes: convection and condensation after Manabe *et al.* (1965); fluxes of sensible and latent heat following a bulk aerodynamic formulation with the assumption of no heat storage over land; and interactions with subgrid-scale motions through horizontal and vertical diffusion. Moisture in excess of 80% relative humidity is precipitated without evaporation of the condensate in intervening layers. See McAvaney *et al.* (1978) for more details.

In the Appendix we derive the model topography which is displayed in Fig. 1a. In Figs. 1b and 1c we show the respective distribution of the fixed, sea-surface temperatures for January and July obtained from Alexander and Mobley (1976). Also shown there are the continental outlines as resolved by the transform grid. The shaded regions depict the areal extent of ice cover for each month. This delineation of land, ocean and ice enters in the treatment of physical processes at the bottom of the atmosphere.

b. Radiation

Detailed descriptions of the radiation and the interactive cloud model are given in Ramanathan *et al.* (1983).

[2] This model is also referred to as the NCAR Community Climate Model–Version 0 (CCM0).

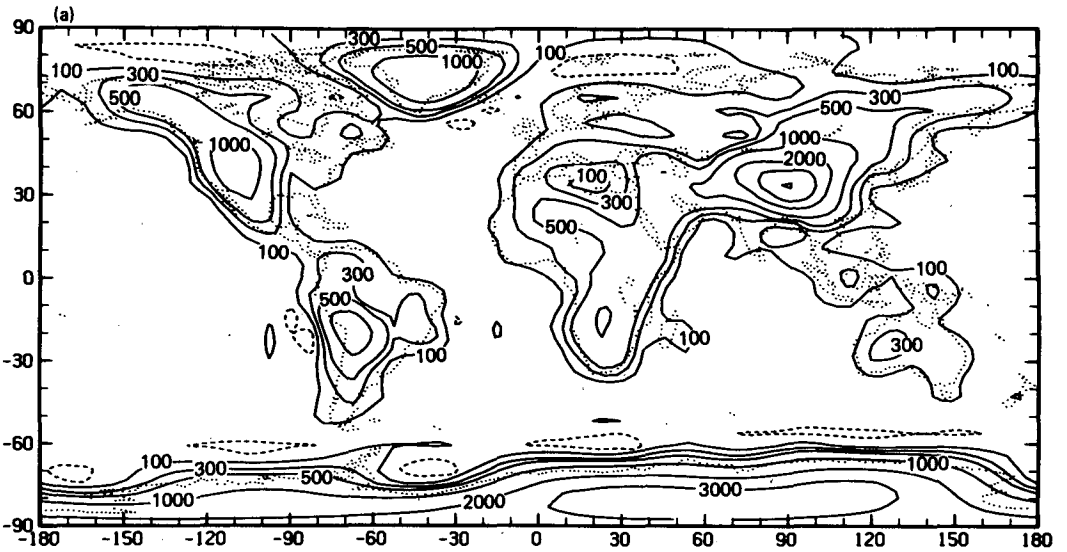

FIG. 1. (a) The topographic heights (m) used in the model simulation. Dashed contours enclose areas less than −100 m. Above 1000 m the contour interval is 1000 m, below 1000 m the contours are 500, 300 and 100 m.

The clear-sky radiative calculation is separated into two parts, shortwave (solar) and longwave (infrared). In addition to Rayleigh scattering, the shortwave component includes absorption by O_3, H_2O, CO_2 and O_2. The longwave component considers absorption and emission by CO_2 (fundamental, first and second hot bands in the 12–18 μm region for the four major CO_2 isotopes), H_2O (rotational [>12 μm], vibration-rotation [4–8 μm], and continuum band [8–12 μm], but *e*-type absorption is neglected), and O_3 (9.6 μm vibration–rotation band). The earth's surface is taken to be non-black (i.e., emissivity < 1) in the 8–12 μm region.

Clouds are formed in the model interactively, and may be of the convective or non-convective type. All levels permit clouds except the lowest one and the top three. If the relative humidity exceeds 80% (the value assumed for saturation), clouds are formed, and the fractional cloud cover depends upon whether the clouds are convective or non-convective. Multiple reflections between cloud layers and between clouds and the surface are accounted for, and clouds are assumed to be randomly overlapped in the vertical. The zenith angle dependence of cloud albedo is included.

c. *Model simulations*

A preliminary version of the model was initialized from real data and integrated for 200 days with perpetual January forcing, i.e., sea–surface temperature, sea–ice distribution and solar zenith angle held constant at their January values. The calculations were interrupted at this stage and modifications were made in the newly installed radiative treatment. Using this final version, the integration was continued for an additional 200 days. The results discussed in this paper are time averages of the final 120 days. The July simulation was started from real data and run for 200 days. The results presented here are from the last 120 days. Extensions of these two standard runs revealed that the model had indeed reached a state of equilibrium.

Observations are most often available in the form of seasonal averages, or as an ensemble mean of many Januaries, for example, whereas the current model results are based on perpetual simulations. Even though it is common to compare perpetual model results with such observations, it is clear that such a comparison is not entirely valid and may not give a completely accurate assessment of how the model might perform were it operated in a mode consonant with nature. To what extent differences between model results and observations may be attributed to running in a perpetual mode is not easily estimated, yet needs to be borne in mind whenever one compares model results of the type presented here with observations.

3. Zonal-mean fields

a. *Zonal wind*

Shown in Fig. 2 are the January and July simulations of the zonal wind, together with observations from Newell *et al.* (1972). The midlatitude tropospheric jets generated by the model are well positioned in both latitude and height, apart from the Northern Hemisphere summertime jet which is situated too far north. The intensities compare favor-

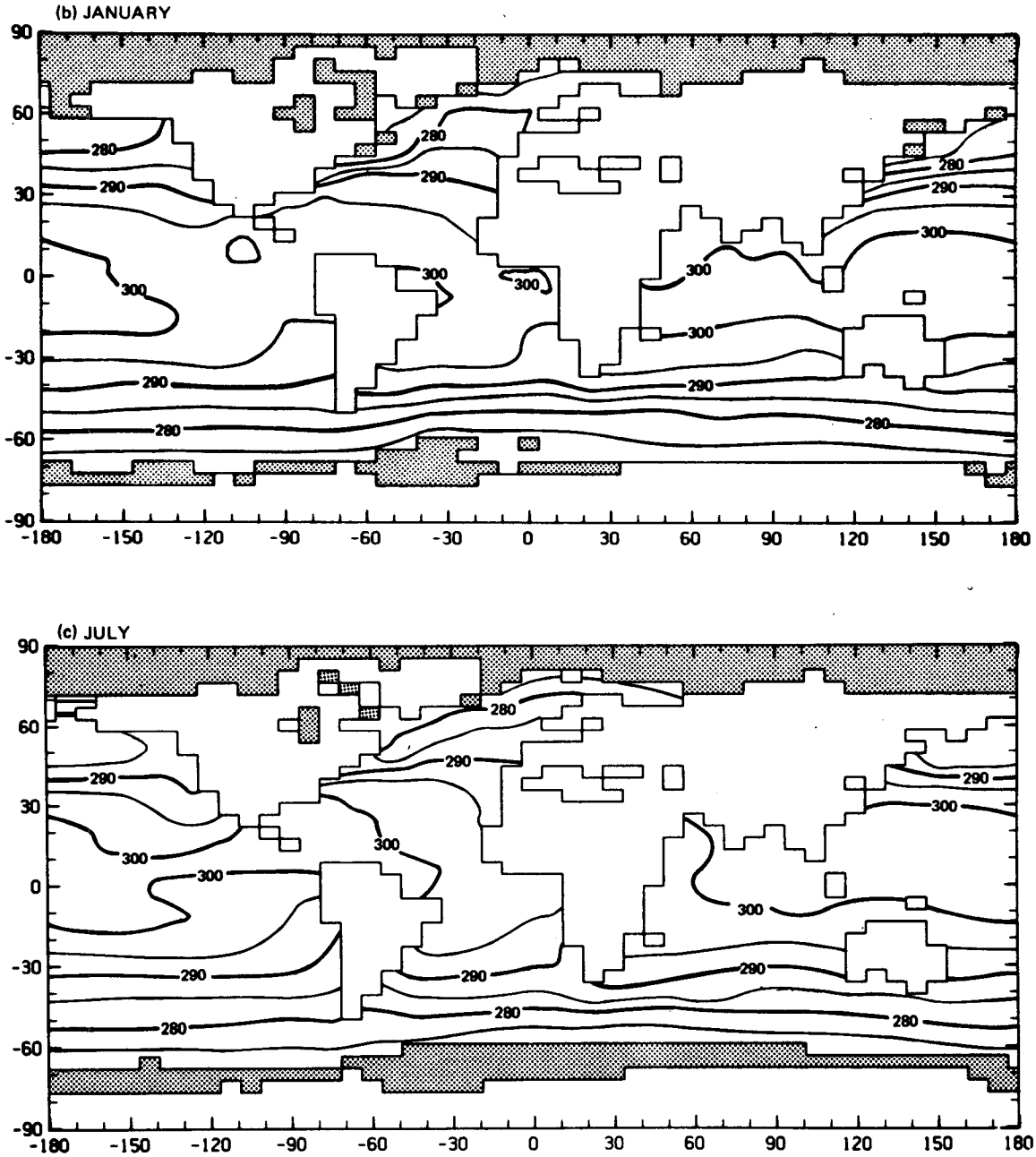

FIG. 1. (b), (c). The sea-surface temperature (K) and land-sea-ice distribution used in the simulation for (b) January and (c) July. The contour interval is 5 K. Stippled areas denote regions of sea ice.

ably with the observations, especially in the winter hemisphere, while the summertime jets are 5 m s^{-1} weaker than observed. As described in Ramanathan *et al.* (1983), if cirrus clouds with non-black emissivity are added at levels 7 and 8, their radiative effects strengthen the summertime jet by about 5–10 m s^{-1}. Such clouds are a contemplated model improvement, but are not present in the model we are discussing here. Notably improved over earlier simulations (e.g., McAvaney *et al.*, 1978) is the closed-off tropospheric jet and the simulation of the polar-night stratospheric jet. The present model produces a separation between the stratospheric and tropospheric jets, and the wind speeds near the top of the model in Northern Hemisphere January are within a few meters per second of the observed. Separation between upper and lower jets in Southern Hemisphere July is not as distinct as in Northern Hemisphere January in either the observations or the model. The model wind speeds at 20 mb and 60°S in July are almost 10 m s^{-1} stronger

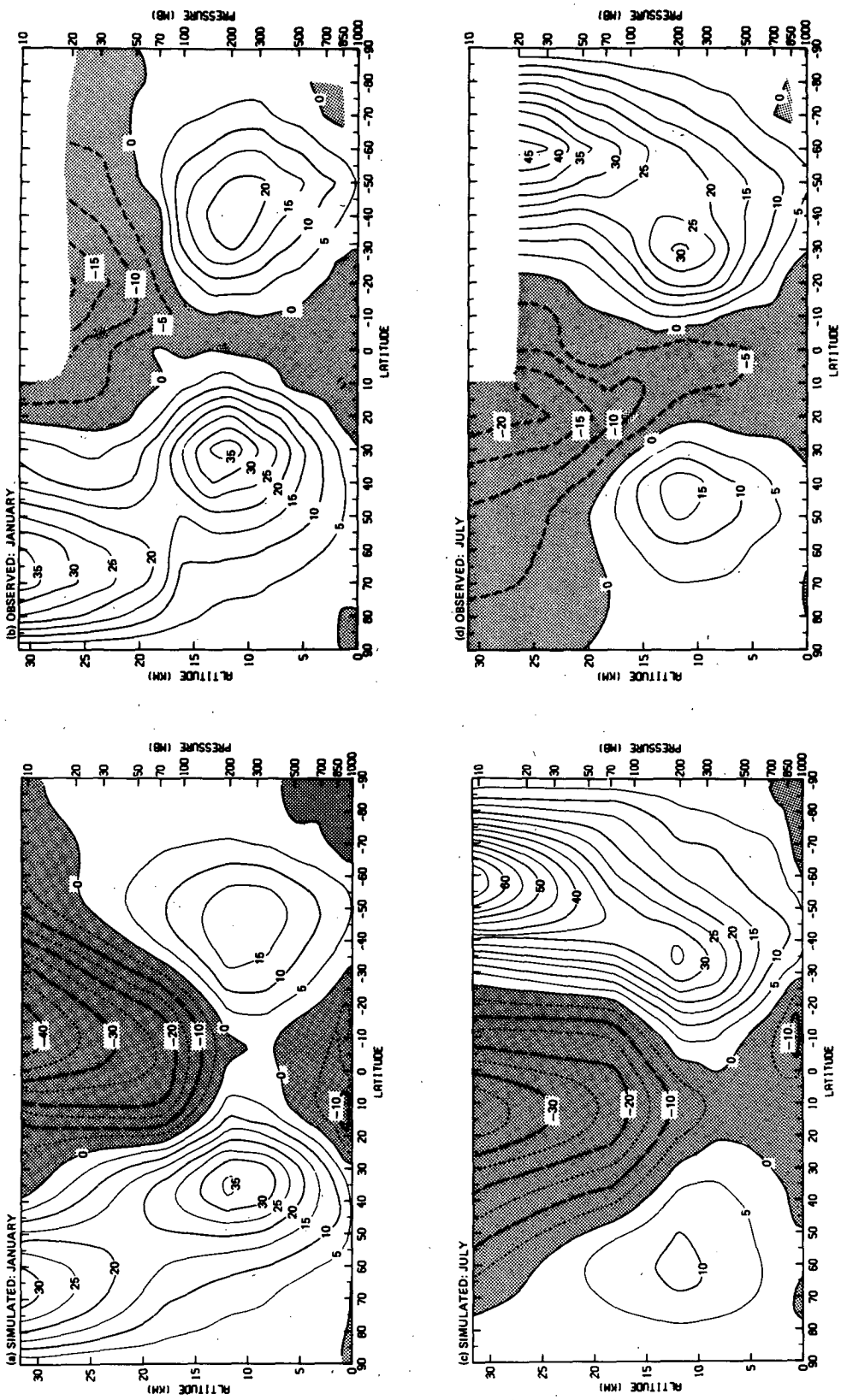

FIG. 2. Zonally averaged zonal-wind component (m s^{-1}) as simulated by the model for (a) January and (c) July. The observations for the (b) December–February and (d) June–August seasons are from Newell *et al.* (1972). Regions of easterly flow (negative sign) are stippled.

than the observations would indicate, though the sparsity of observations in this region may, in part, account for the discrepancy. A deficiency which still remains is the excessive speeds of the tropical easterlies, by 5 m s^{-1} at the surface and 10–15 m s^{-1} in the stratosphere. On the other hand, weak surface easterlies are simulated in the polar regions in agreement with observations.

Reasons for the overall success of the zonal-wind simulations are explored in Ramanathan *et al.* (1983), to which the reader is referred for a complete discussion. That paper serves to identify four temperature- and latitude-dependent radiative processes which, upon inclusion in this model, tend to reduce the equator-to-pole gradient of net radiative heating in the troposphere/stratosphere system. This leads by way of the thermal wind equation to reduced zonal-wind speeds in the upper troposphere and lower stratosphere from those found in the model when these processes are absent. But in addition, it is also shown that northward heat transports by planetary waves into the winter polar stratosphere can be as important as the accurate treatment of radiative processes in determining temperatures there.

b. Temperature

The simulated zonally averaged temperatures for January and July are given in Fig. 3, together with observed values. The model has reproduced the main features contained in the data. In light of the successful zonal-wind simulation, one would expect the meridional temperature gradient to be satisfactorily reproduced by the model. This is indeed the case. The principal deficiency of the simulation is that the troposphere and stratosphere are too cold by 3–7 K. Again, when high-level cirrus clouds with non-black emissivity are added to this model (Ramanathan *et al.*, 1983), the tropical upper troposphere warms by about 3–5 K and the lower troposphere warms by 1–2 K. The temperatures in the polar–night stratosphere agree with those observed to within a couple of kelvins, and this agreement manifests itself in the moderate wind speeds simulated in the polar jet as discussed earlier. The model is successful in simulating the polar surface–temperature inversion in January. The quality of the simulation is roughly the same for both January and July.

c. Meridional wind

The simulated and observed zonally averaged meridional winds are displayed in Fig. 4. The most pronounced feature in the observations is the upper branch of the winter hemisphere Hadley cell, and the simulation is successful in capturing the location of the maximum in poleward flow, but in January the intensity is underestimated by 1.5 m s^{-1} in comparison with that observed. The mean meridional motions are asymmetric, displaying greater strength in the winter hemisphere, and the simulation also possesses this feature. The model-generated wintertime equatorward flow at low latitudes near the ground—the low-level branch of the Hadley cell—is too swift. The remaining meridional flow patterns qualitatively agree with the observed features apart from the Northern Hemisphere polar regions in both January and July. A detailed comparison of this quantity with observations is difficult owing to the uncertainties present in the observations themselves. This is convincingly shown by Lau and Oort (1981) who found for the Northern Hemisphere meridional flow that the difference between two analyses obtained by two techniques is comparable to the meridional flow itself.

d. Vertical velocity

Fig. 5 shows the zonal average of the simulated vertical velocity $\omega = dp/dt$, together with observations for January and July. The ascending and descending branches of the wintertime Hadley circulation are well positioned in the simulation though slightly narrow in latitudinal extent and somewhat too vigorous. Taken together, Figs. 4 and 5 show a three-cell pattern in the meridional plane in each hemisphere for both January and July. The meridional overturning in the model is weaker in the summertime hemisphere in keeping with the observations. Vincent (1968) observed a broad region of descending motion in the stratosphere, centered about the Northern Hemisphere midlatitudes in January, as well as regions of ascent to the north and south. These features are present in the simulation, and are indicative of the thermally indirect circulations observed in the stratosphere in Northern Hemisphere January. The northern edge of ascent in the model stratosphere near 25°N moves poleward in July from its position in the January simulation, a feature which also appears in the observations (Vincent, 1968) though to a greater degree.

4. Geographical distributions

a. Sea-level pressure

Fig. 6 depicts the global distribution of sea-level pressure from the model along with observations for January and July from Schutz and Gates (1971, 1972b). Model surface-pressures have been extrapolated to sea level by assuming hydrostatic balance and a temperature lapse rate of 6.5 K km^{-1}.

The January simulation is successful in capturing most of the features appearing in the climatological chart. The strength and position of the Icelandic low compare favorably with the observations, with its simulated eastward extension somewhat south of the observed trough axis. The Aleutian low is well sim-

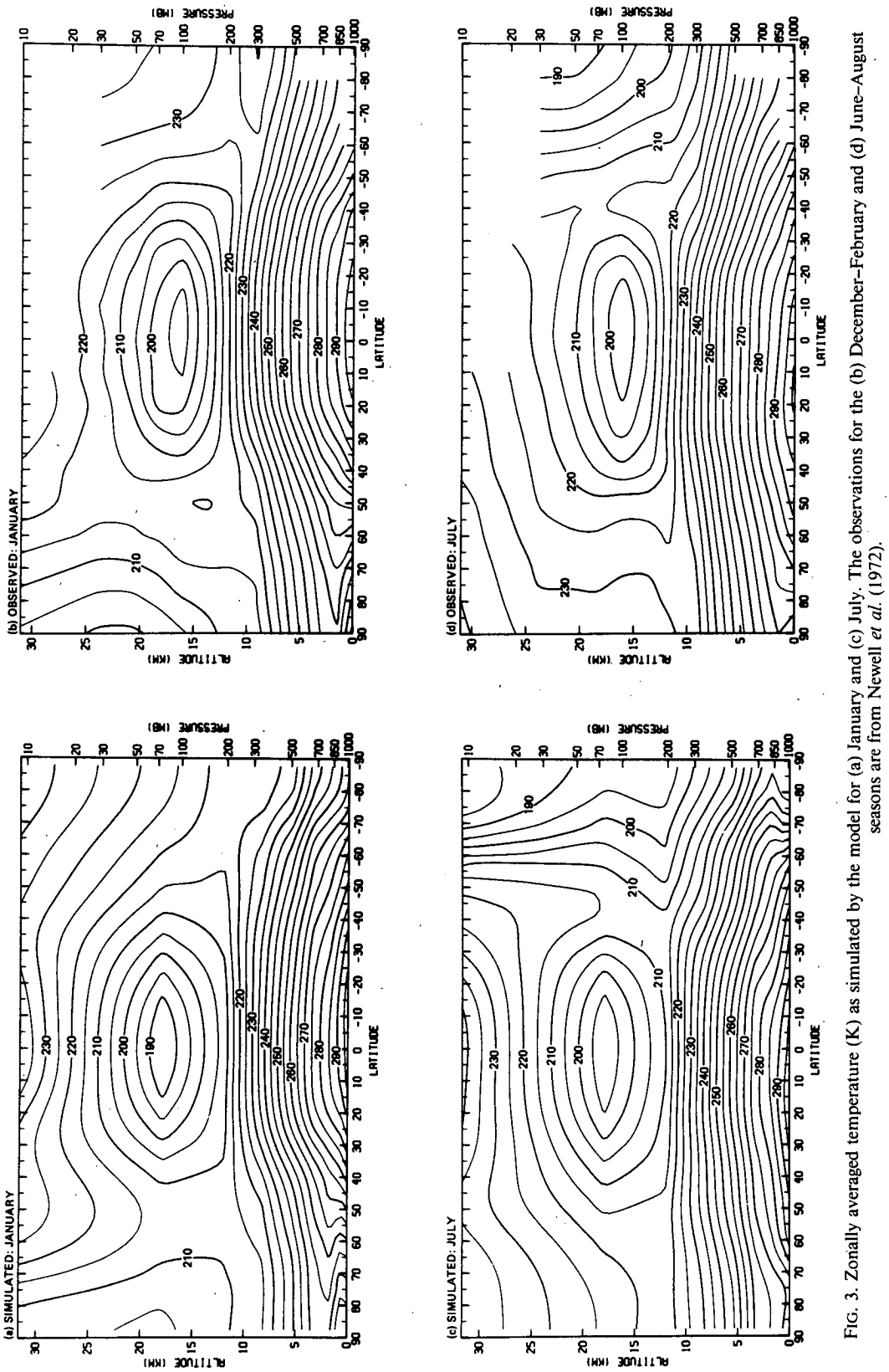

FIG. 3. Zonally averaged temperature (K) as simulated by the model for (a) January and (c) July. The observations for the (b) December–February and (d) June–August seasons are from Newell *et al.* (1972).

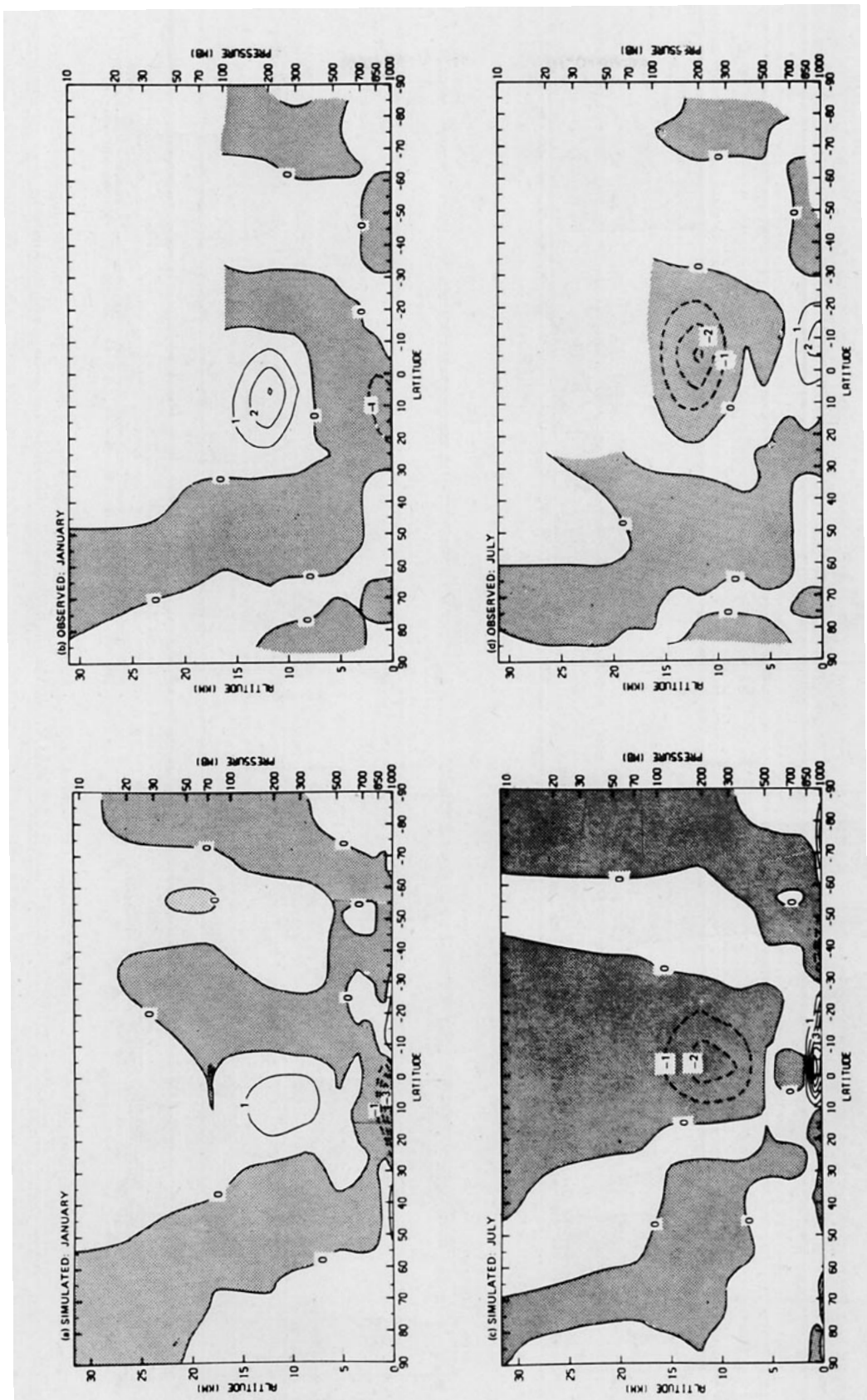

FIG. 4. Zonally averaged meridional-wind component (m s^{-1}) as simulated by the model for (a) January and (c) July. The observations for the (b) December–February and (d) June–August seasons are from Newell *et al.* (1972). Regions of northerly flow (negative sign) are stippled.

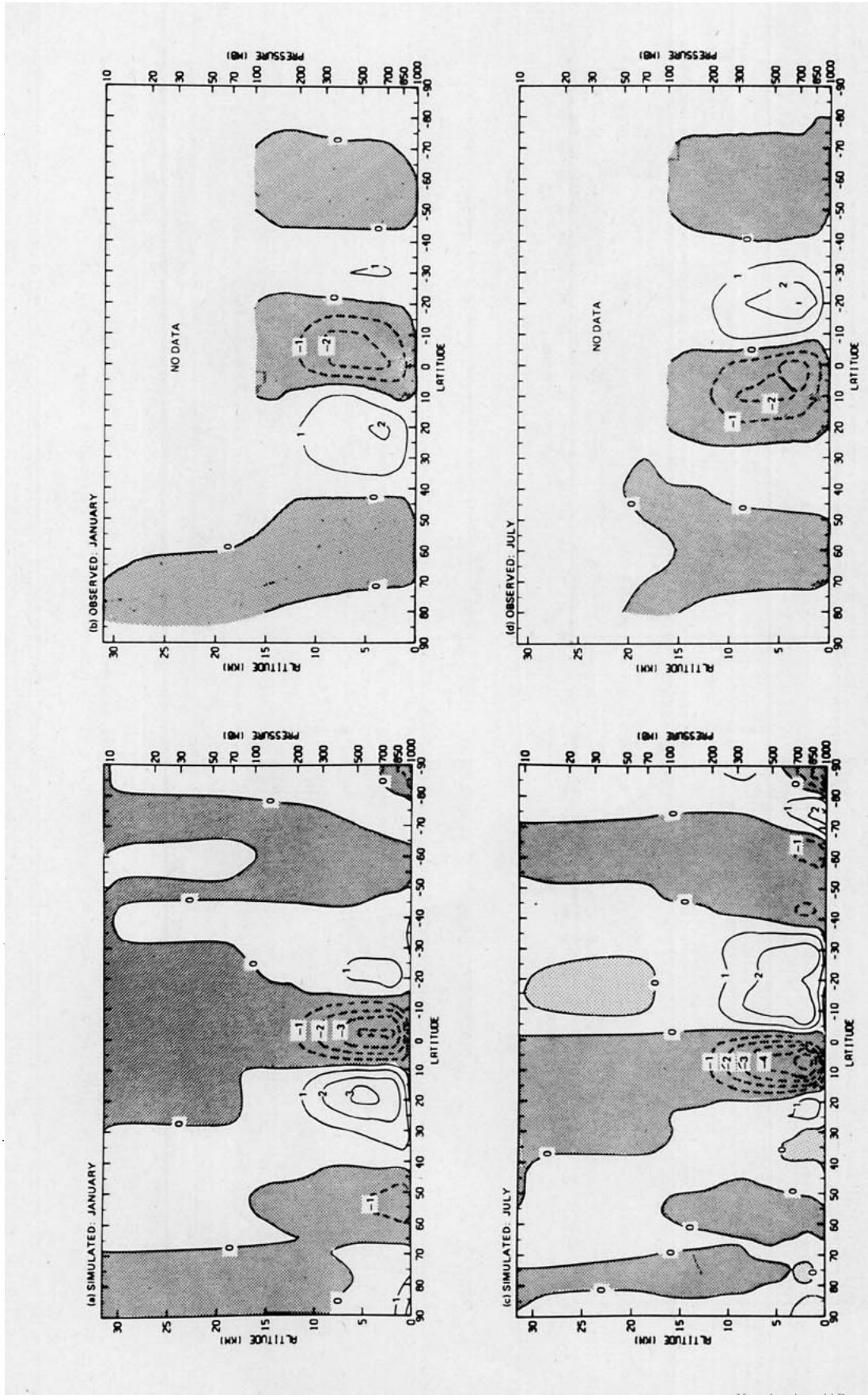

FIG. 5. Zonally averaged vertical velocity in pressure coordinates (10^{-4} mb s^{-1}) as simulated by the model for (a) January and (c) July. The observations for the (b) December–February and (d) June–August seasons are from Newell *et al.* (1972). Regions of upward motion (negative sign) are stippled.

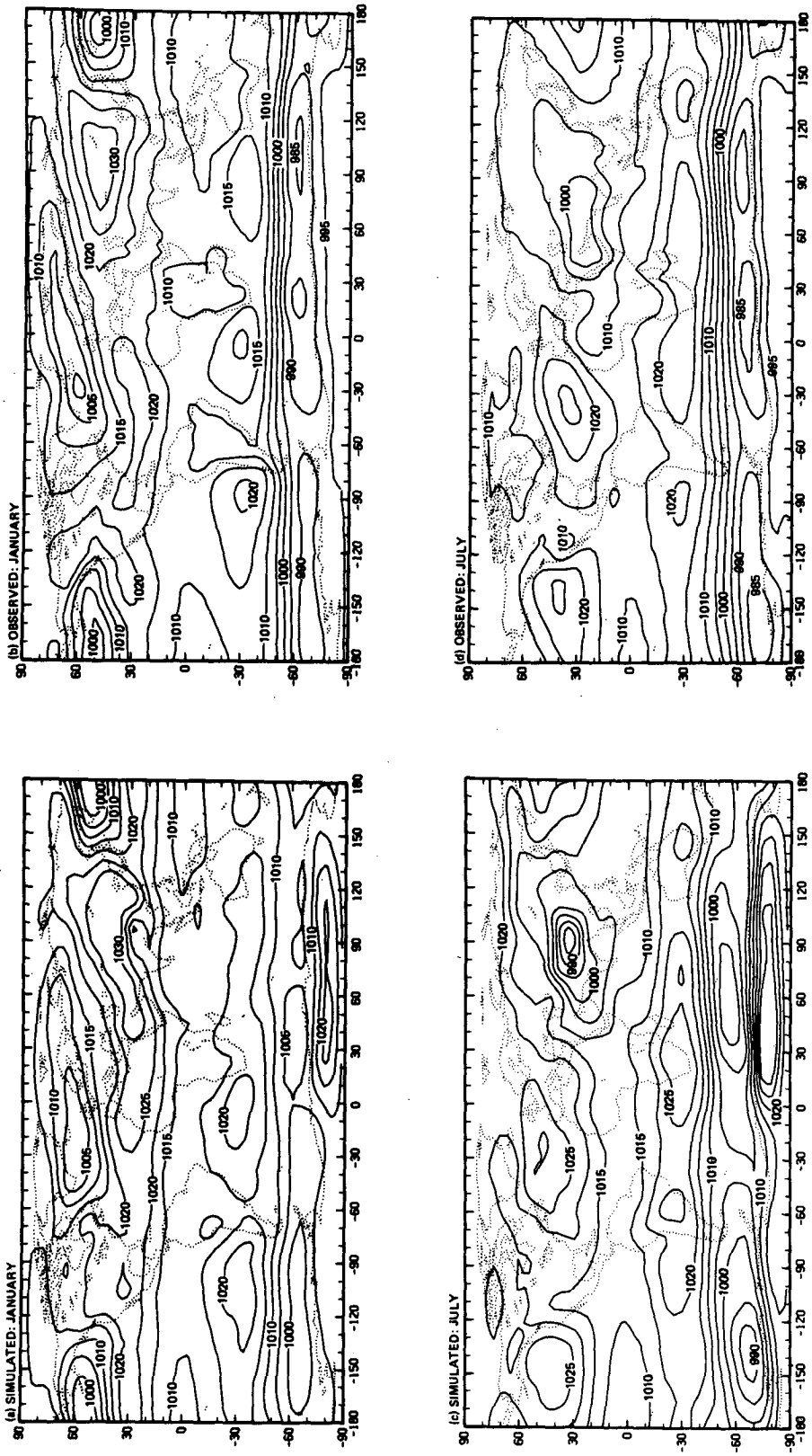

FIG. 6. Sea-level pressure (mb) as (a) simulated by the model and (b) observed for January, and as (c) simulated and (d) observed for July. The observations for January are from Schutz and Gates (1971), those for July from Schutz and Gates (1972b).

ulated, appearing near the international dateline as a single center of low pressure, while the observations suggest an elongated minimum in the pressure field centered about this mean position. The Siberian high present in the model is well positioned in longitude and about 7° south of the observed center. It is too intense by about 5 mb. The westward extension of the high-pressure ridge into the Middle East and North Africa is not in agreement with the observations. [A similar feature may be seen in McAvaney *et al.* (1978) and Manabe and Hahn (1981).] The model does capture the broad equatorial belt of low pressure, and positions the subtropical high-pressure systems to the west of continents in the Southern Hemisphere. The climatological low-pressure troughs over South America and Africa are evident in the simulation but to a much lesser extent. We believe that this last deficiency is a direct result of the prescription of surface evaporation and shall return to this in the next subsection. The model properly locates the circumpolar Antarctic trough, but underestimates its intensity by some 10–15 mb.

In the July simulation the centers of the North Atlantic and Pacific high-pressure systems are properly located west of the principal land masses, but the centers are 5–10° too far north and 5 mb too high. The model generates an Arctic zone of high pressure which is not observed. The Indian monsoon is well developed in the model, perhaps even more vigorous than the observations would indicate, while the center of the low is displaced several degrees to the east of its climatological position. Over South America and Africa are found regions of excessive high pressure in the simulation. These features appear to be counterparts to the continental subtropical high pressures occurring in the Northern Hemisphere January simulation, and their existence remains unexplained. Central pressures associated with the Antarctic circumpolar trough are closer to that observed in the July simulation, yet the centers are about 7° too far north. Perhaps the smoothed topography in the model is effectively acting as a barrier to the intrusion of cyclonic disturbances. Excessive pressures over Antarctica, where the model is found to simulate strong surface-temperature inversions, may, in part, be an artifact of surface-pressure reduction to sea level.

b. Surface air temperature

Shown in Fig. 7 is the surface air temperature, simulated and observed, for January and July. The model temperatures have been computed by extrapolation from the two lowest σ-levels (0.991, 0.926) to $\sigma = 1.0$, a distance of some 80 m, using the model lapse rate and the hydrostatic assumption. Since the temperature of the ocean surface is prescribed, it is reasonable to expect good agreement between simulated and observed surface air temperature over oceanic regions. Elsewhere, the shape of the temperature contours well represents the patterns evident in the observed fields. For example, in January the temperature minima in Siberia and northern Canada are reproduced by the model. Closer examination reveals that the temperatures over continents in the model are systematically lower than that observed. This even holds true in the high Arctic in the January simulation where the surface air temperature is 5–10 K lower than observed. By way of contrast, an earlier version of this model (McAvaney *et al.*, 1978) as well as the spectral model described by Manabe and Hahn (1981) show temperatures in this region to be too warm by about the same amount.

In July many of the principal features in the surface air temperature are reproduced by the model, including the minima over Greenland, the Himalayas, western South America and southeastern Africa. With the exception of Antarctica, where the model temperatures are somewhat warmer than observed, the continental regions, as simulated by the model, tend to be a few degrees cooler than observed. As mentioned earlier, some of the model's bias toward lower temperatures disappears when radiative effects of cirrus with non-black emissivity are added to the basic model described here.

We shall not engage here in a discussion of the several mechanisms which have a controlling influence on the surface temperature, and how their treatment might be improved to yield a more realistic simulation. Rather, we would just like to point out how one of these mechanisms, the evaporation of water from the land surface, can play a decisive role in the determination of air temperature near the ground. Surface evaporation is currently handled through the application of a simple bulk formula (McAvaney *et al.*, 1978), that does not take into account varying soil moisture. Evaporation from the land surface is taken to be 0.25 times the value that would have resulted had the underlying boundary been the ocean surface instead. The use of such a constant "wetness factor" is, no doubt, physically unrealistic in arid regions and tropical rain forests alike. In order to estimate the potential effect that such a formulation might have on the simulation, we performed a January run in which the wetness factor over land was set to zero in the latitude belt 11–39° in both hemispheres. In response to this change a noticeable warming over subtropical continental regions was evident with a marked warming at the surface of some 7–10 K over these regions in the summer hemisphere. The effect of suppressing surface evaporation from the land showed up in other fields as well. For example, the sea-level pressure map showed a substantial intensification of the thermal lows over the principal land masses in the Southern Hemisphere subtropics. As one might expect, the greatest

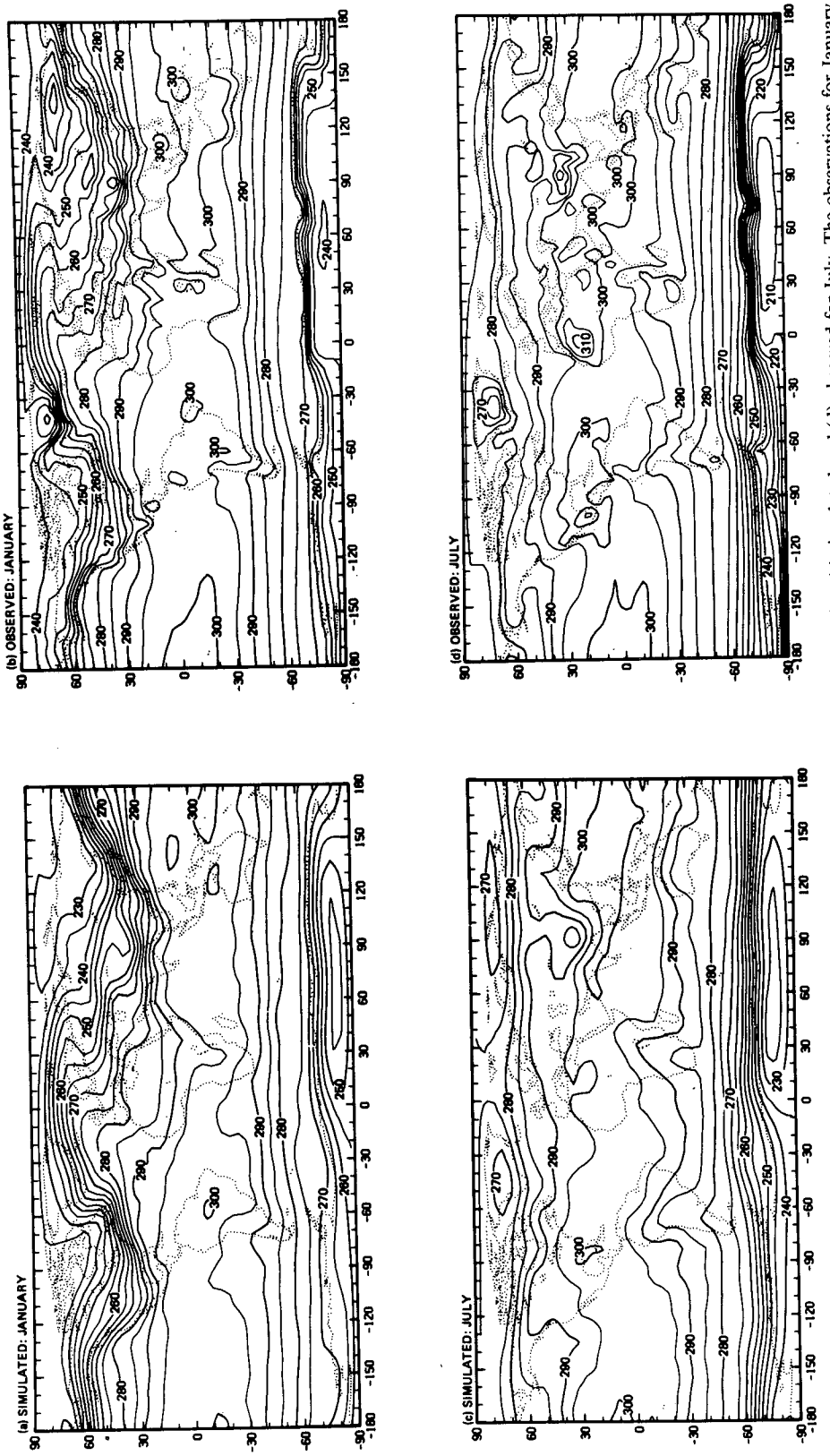

FIG. 7. Surface air temperature (K) as (a) simulated by the model and (b) observed for January, and as (c) simulated and (d) observed for July. The observations for January are from Schutz and Gates (1971), those for July from Schutz and Gates (1972b).

differences between the control run and the one just described were found in the lowest model levels over subtropical land areas.

We have briefly reported upon one experiment to illustrate how the parameterization of one physical process, surface evaporation in this case, can have a substantial influence on the model results. Perhaps more importantly, it highlights the need for an improved treatment of surface hydrology before one can expect to realize the model's potential capability.

c. *Precipitation*

The model's mean-daily precipitation rate for January and July appears in Fig. 8, along with the observed mean for each season centered on these two months. In January the model is successful in reproducing many of the general features found in the observations. For example, the intense equatorial rain belts, including the elongated twin maxima on each side of the equator in the eastern tropical Pacific, the maxima east of North America and Asia, associated with the storm tracks in the North Atlantic and Pacific, the minima over central North America and North Africa, and to a lesser extent the subtropical oceanic minima to the west of continents are located by the model in about the right positions with approximately the correct relative strengths. It is interesting to note that the model is able to simulate the minima over the North African deserts, in spite of the fact that the wetness factor for evaporation in the model is the same over all land areas. There is still room for improvement, however. The precipitation rate in the model generally tends to be somewhat larger than observed, and the delineation of both rainy and arid regions is approximate in some cases, as evidenced by the rainfall maximum situated by the model in northeast Brazil instead of in the heart of the continent. The July simulation shows similar strengths and weaknesses. The model situates an elongated maximum over India and Burma in accordance with the Asian monsoon circulation. The subtropical dry zones are evident in the simulation, as are the tongue of moderate rainfall in the southeast Pacific, extending from the equator, and the midlatitude maximum in the Southern Hemisphere. Unfortunately, the model shows an intense rainfall maximum in the equatorial Atlantic, whereas the observations show this to be an area of moderate rainfall flanked on each side by centers of heavy rainfall over the Amazon jungle and Ivory Coast.

Given that precipitation tends to possess large spatial and temporal variability, better agreement with observations might result were the averaging interval increased. We have noticed that the field of precipitation does vary somewhat from one 120-day period to the next. No doubt, as mentioned earlier, the use of a constant wetness factor instead of a more realistic surface hydrology misrepresents evaporation from the land surface (and consequently affects the supply of moisture available for rainout). On the other hand, increased resolution may be necessary before a significant improvement can be realized. Manabe *et al.* (1979) found that increasing the model resolution led to an improvement in the simulation of precipitation for the GFDL spectral model, however, their high resolution model was run only for a limited period, and so may not have reached equilibrium, and hence further experimentation may be necessary.

d. *500 mb vertical velocity*

The simulated 500 mb vertical velocity transformed to pressure coordinates and multiplied by -1 is given in Fig. 9 for January and July. In January the topographic forcing in the Northern Hemisphere is quite apparent, with rising motion windward of the Rockies, the Greenland icecap and the Tibetan plateau, and with subsidence leeward of these geographical features. Broad areas of upward motion in the North Atlantic and Pacific are consistent with the presence at the surface of the Icelandic and Aleutian low-pressure systems. The intertropical convergence zone (ITCZ) is seen to wind its way principally through the southern reaches of tropical latitudes in general agreement with observations (Newell *et al.*, 1974). Of interest is the association between heavy precipitation and enhanced rising motion over the equatorial continents and Indonesia, a relationship also found in the atmosphere. In the Southern Hemisphere there exists subsidence over the relatively cool subtropical oceans to the west of the major land masses, while upward motion prevails at the southernmost latitudes adjacent to Antarctica where we find the circumpolar pressure trough at the surface.

The July simulation shows the expected northward migration of the ITCZ, and the relationship between centers of rising motion and abundant rainfall in the tropics is still evident. In this regard it should be noted that, as with the maximum in precipitation found in the model northeast of Brazil, the model incorrectly locates a center of rising motion there also. In the atmosphere, on the other hand, there are found two centers of upward motion in this general region—one about 25° to the east, and another, smaller center situated near Panama (Newell *et al.*, 1974). The dynamical influence of midlatitude topography in the summer hemisphere is diminished, and we now find broad regions of subsidence over the cooler waters of the eastern Pacific and Atlantic. Upward (downward) motion west (east) of the Andes, and subsidence over southern Africa and the Indian ocean are also found in the data of Newell *et al.* (1974).

e. *500 mb height*

We present in Fig. 10 the wintertime 500 mb geopotential height together with observations for the

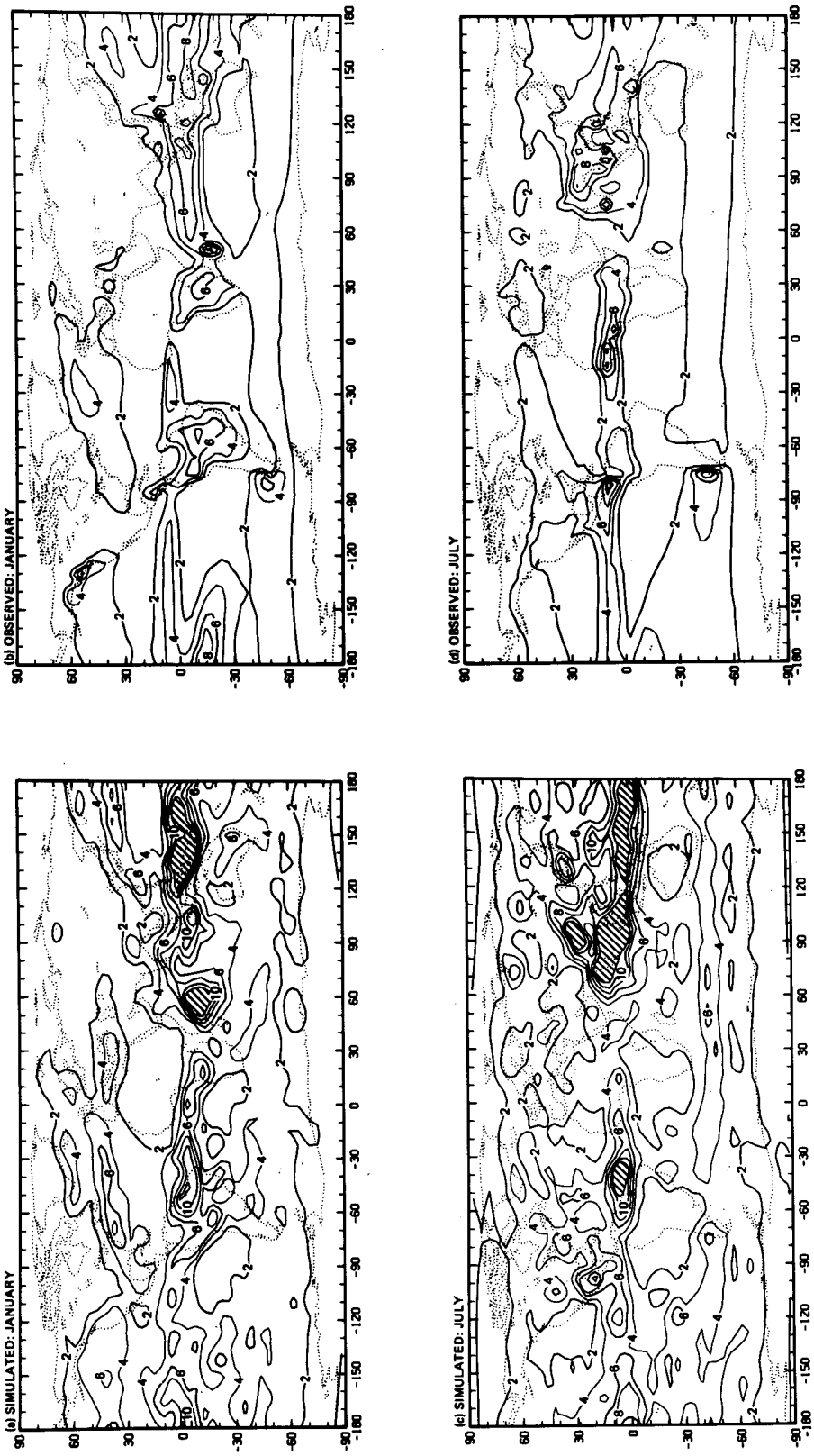

FIG. 8. Precipitation rate (mm day^{-1}) as simulated by the model for (a) January and (c) July. The observations for the (b) December–February season are from Schutz and Gates (1972a); those for the (d) June–August season are from Schutz and Gates (1972b). Regions with values in excess of 12 mm day^{-1} are cross-hatched.

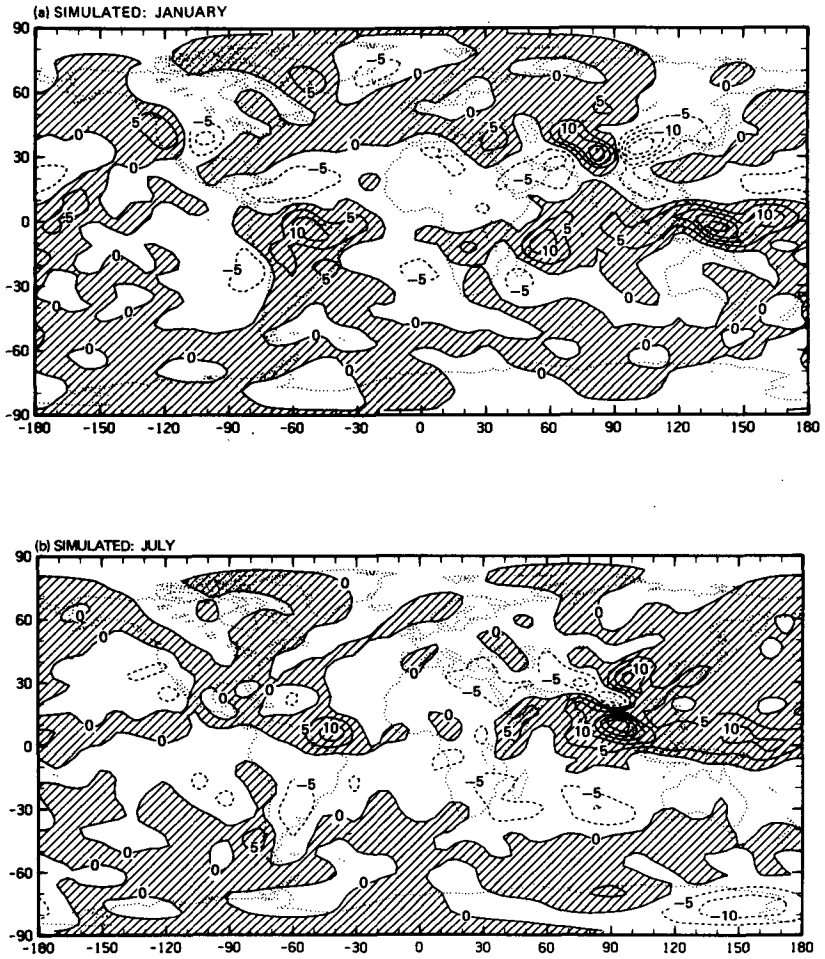

FIG. 9. The negative of the vertical velocity in pressure coordinates (10^{-4} mb s^{-1}) as simulated by the model for (a) January and (b) July. Regions of upward motion (positive sign) are cross-hatched.

Northern (Blackmon, 1976) and Southern Hemispheres. The observations for the Southern Hemisphere are based on the final operational analyses of the Australian Weather Bureau for the period 1962/63–1979/80. In January, pressure troughs over the east coasts of Asia and North America dominate the 500 mb height field in both the observations and the simulation. The third trough over eastern Europe and the weak pressure ridge downstream are also captured by the model. The observed ridge in the North Atlantic and the one over the Bering Strait appear in the simulation, though the model locates the second of these over eastern Alaska. Overall, the large-scale stationary features are faithfully represented in the model, the main deficiency being that the 500 mb surface is systematically too low. This is consistent with the colder-than-observed tropospheric temperatures commented on previously.

Both the observations and model calculations reveal smaller-amplitude stationary features at 500 mb during the Southern Hemisphere winter. Closer examination, however, does show departures from zonal symmetry. There is an observed, strong midlatitude gradient in the height field near 40–60°E, and this feature is also present in the July simulation. The weak trough east of South America is reproduced by the model, as are the three, more prominent troughs embracing Antarctica. Like the Northern Hemisphere January simulation though, the 500 mb surface, at least in the subtropics and midlatitudes, is lower than observed for the Southern Hemisphere July case as well.

f. 300 mb zonal wind

Shown in Fig. 11 is the 300 mb westerly wind component in the winter hemisphere as computed by the model for January and July, and as observed for a multiyear four-month winter season. The observations for the Northern Hemisphere are derived from

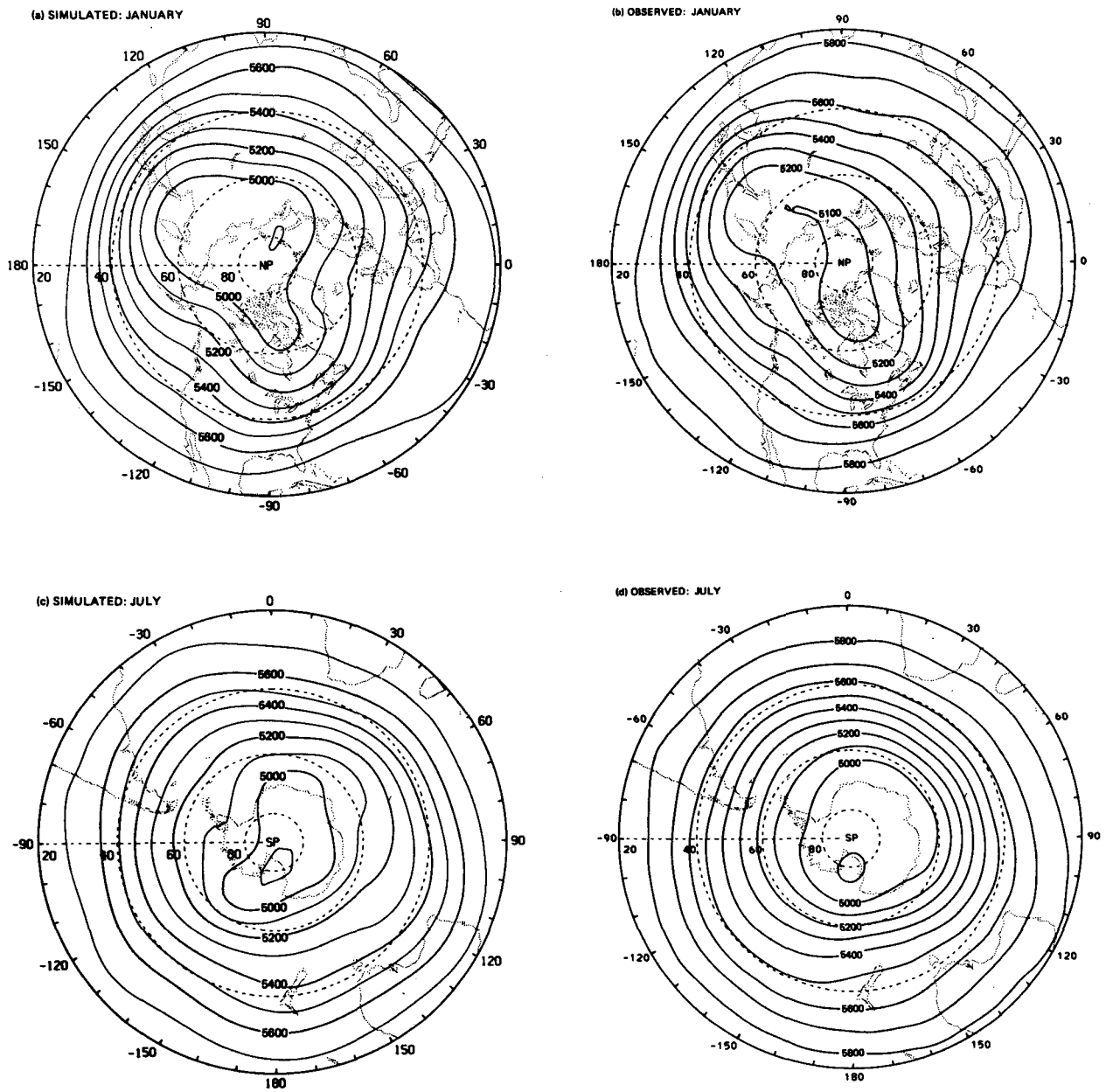

FIG. 10. Geopotential height (m) at 500 mb as simulated by the model for (a) January, north of 20°N and (c) July, south of 20°S. The observations for the (b) mid-November–mid-March period are from Blackmon (1976); those for the (d) mid-May–mid-September period are from the analyses of the Australian Weather Bureau for the period 1962/63–1979/80.

the data of Lau *et al.* (1981), and for the Southern Hemisphere we use the Australian analyses cited above. Two prominent jet maxima exist in both the atmosphere and the model in the Northern Hemisphere. The Asian jet has its origin over North Africa in the model, spirals gently poleward, and reaches a maximum east of Japan in good agreement with observations. The model also faithfully simulates the strength of the jet stream over the United States and properly positions the jet axis.

Blackmon *et al.* (1977) discuss the energetics of jet streams in the Northern Hemisphere. Based on their observational study, they postulate the existence of two secondary circulations: 1) a thermally direct circulation dominating in the upstream "entrance" region of the jet stream, and 2) a thermally indirect circulation dominating in the downstream "exit" region of the jet. In support of this hypothesis, they show the ageostrophic wind component normal to the geostrophic wind at 250 mb and interpret this as

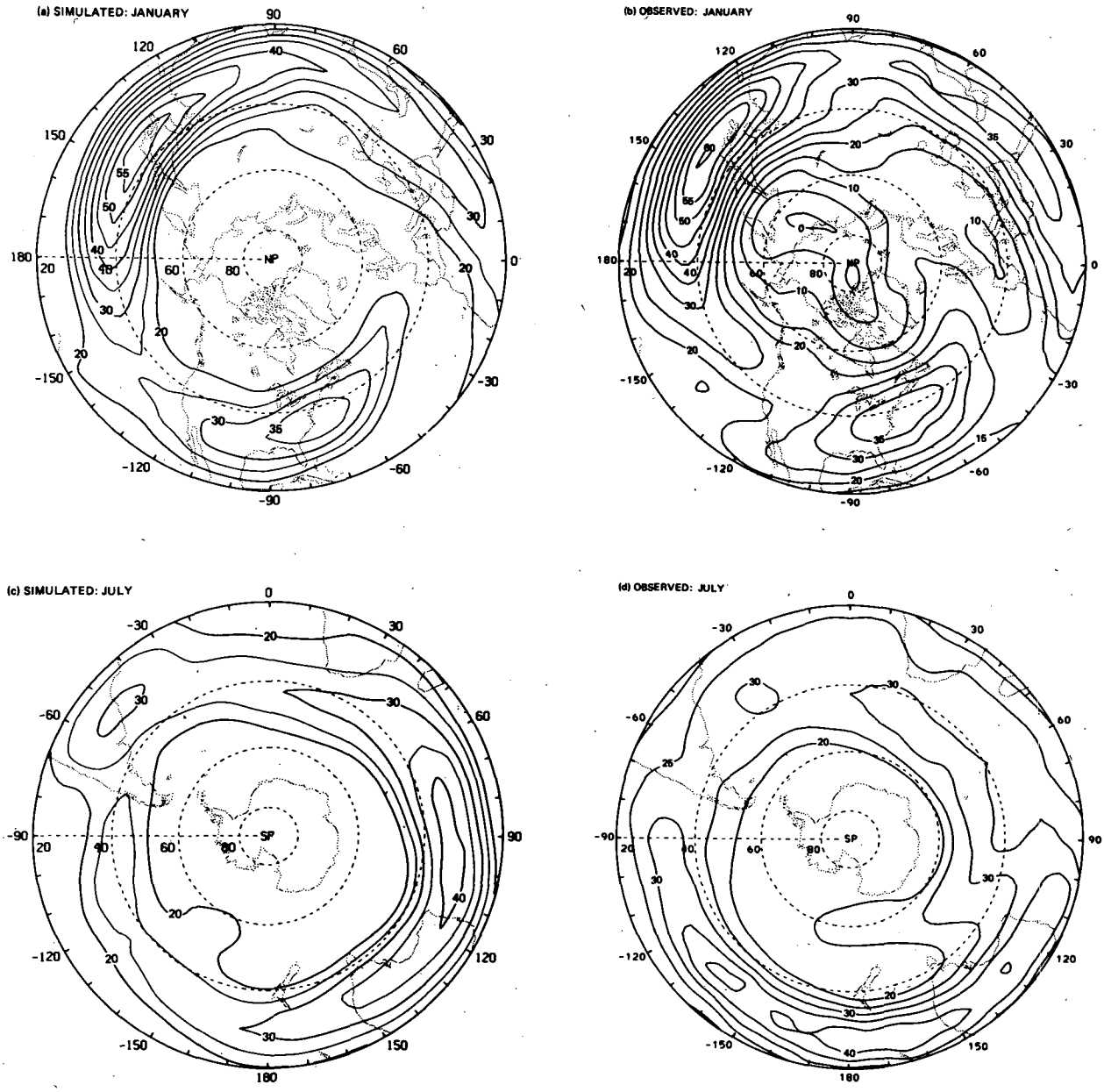

FIG. 11. Zonal-wind component (m s^{-1}) at 300 mb as simulated by the model for (a) January, north of 20°N and (c) July, south of 20°S. The observations for the (b) mid-November–mid-March period are from Lau *et al.* (1981); those for the (d) mid-May–mid-September period are from the analyses of the Australian Weather Bureau for the period 1962/63–1979/80.

the upper branch of thermally direct or indirect circulation transverse to the jets. They find the cross-isobar flow upstream from the major jet streams to be poleward, while equatorward flow dominates in the downstream region. Furthermore, Lau (1978) finds that, based upon the evaluation of the principal terms in the time-averaged zonal momentum equation, the ageostrophic flow plays a locally dominant role in the maintenance of the zonal wind.

In Fig. 12 we show the northward component of the ageostrophic wind from the model at 300 mb for January, along with the observed seasonal average taken from the data of Lau *et al.* (1981). There is a clear, qualitative agreement between the model and the atmosphere in the two broad sectors centered on the east coasts of Asia and North America. Comparison with Fig. 11a reveals that the model does possess the expected poleward flow in the accelerating regions of the two major jet streams, and equatorward flow downstream in the decelerating regions.

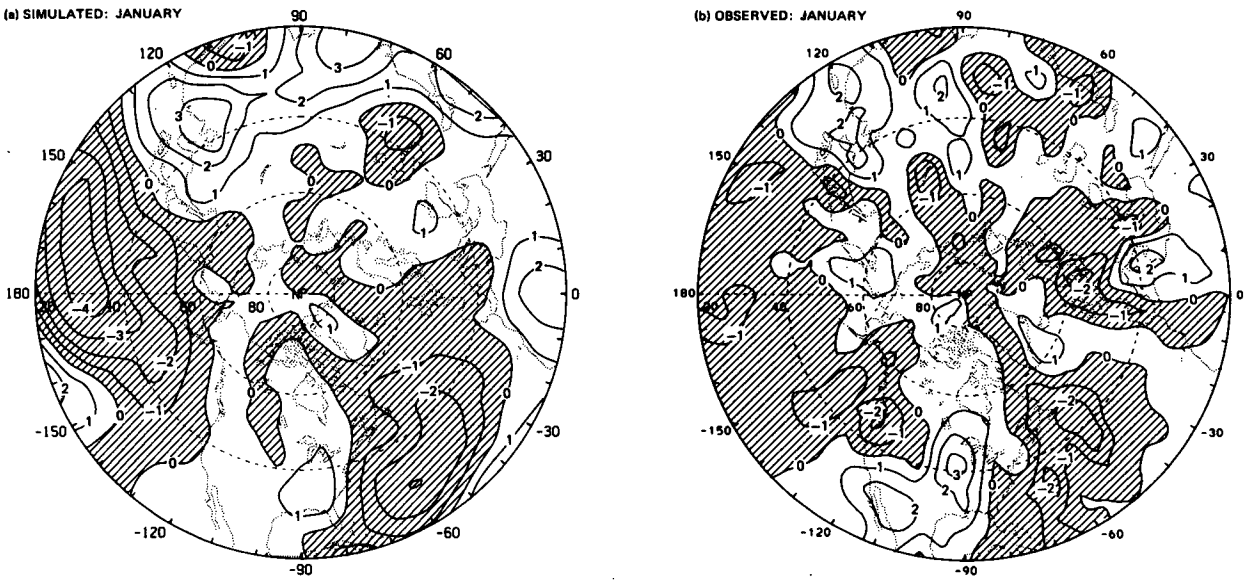

FIG. 12. Northward component of the ageostrophic wind (m s^{-1}) at 300 mb as (a) simulated by the model for January and as (b) observed for the mid-November–mid-March period from Lau *et al.* (1981).

We turn now to the distribution of the zonal wind at 300 mb in the Southern Hemisphere for the model (Fig. 11c) and the atmosphere (Fig. 11d). The observations in July are characterized by two major jet streams like that of the Northern Hemisphere winter. Unlike the Northern Hemisphere, where the major jet cores are equatorward of 40°N, the Southern Hemisphere exhibits a subtropical jet at 25–30°S with two (for the observations shown here) jet cores downstream of Australia, and a higher latitude jet having its origin east of South America, extending eastward across the Indian ocean at 50°S, and decaying poleward of New Zealand near 60°S. This is in general agreement with Physick (1981) who performed an observational study of the 1979 winter during the FGGE observing period in which TIROS-N satellite data are available. The model does simulate a subtropical jet, although the jet core is located upstream from Australia and about 5° poleward of that observed, but the higher latitude jet appearing in the atmosphere is not present in the simulation. We have examined other averaging intervals from extended integrations with the model, and conclude that the result shown here is representative of the model's behavior and not an anomalous fluctuation. The reason for this shortcoming has not yet been identified.

g. 100 mb temperature

It is well known that the general circulation of the stratosphere possesses several distinctive features which distinguish it from the troposphere [see Holton (1975) for a summary of the observational evidence and an extensive bibliography]. Indeed, even within the stratosphere itself there are found substantial variations between the two winter hemispheres, between summer and winter, and between the upper and lower levels. Such variations have been investigated with the aid of general circulation models (Manabe and Mahlman, 1976; O'Neill *et al.*, 1982). It is beyond the intent of the present paper to give a detailed account of the model's performance in simulating the stratospheric circulation; rather, we wish to show in this and the next subsection a limited number of fields to give the reader some measure of the model's ability to capture the major features of the stratosphere. Of the nine levels in the vertical, three are located in the model stratosphere (σ = 0.189, 0.074 and 0.009). We show the 100 mb temperature as computed by the model (Fig. 13a) for Northern Hemisphere January, and as observed for the winter season (Fig. 13b) after Lau *et al.* (1981). Both the model and the atmosphere are characterized by the presence of a midlatitude "warm belt" in the region where the thermally indirect meridional circulation is characterized by subsidence (Fig. 5). The model correctly positions a maximum in the thermal field over Kamchatka, and approximately captures the position of the polar minimum, whose central value in the simulation is within 3 K of that observed. A midlatitude maximum is simulated in Southern Hemisphere July (Fig. 13c) some 10° equatorward of its Northern Hemisphere counterpart and, moreover, displays a greater degree of zonal symmetry. Each summer hemisphere in the model result (not shown) is characterized by a more-or-less steady increase in temperature from the equator (~193 K) to a maximum (~223 K) near the pole.

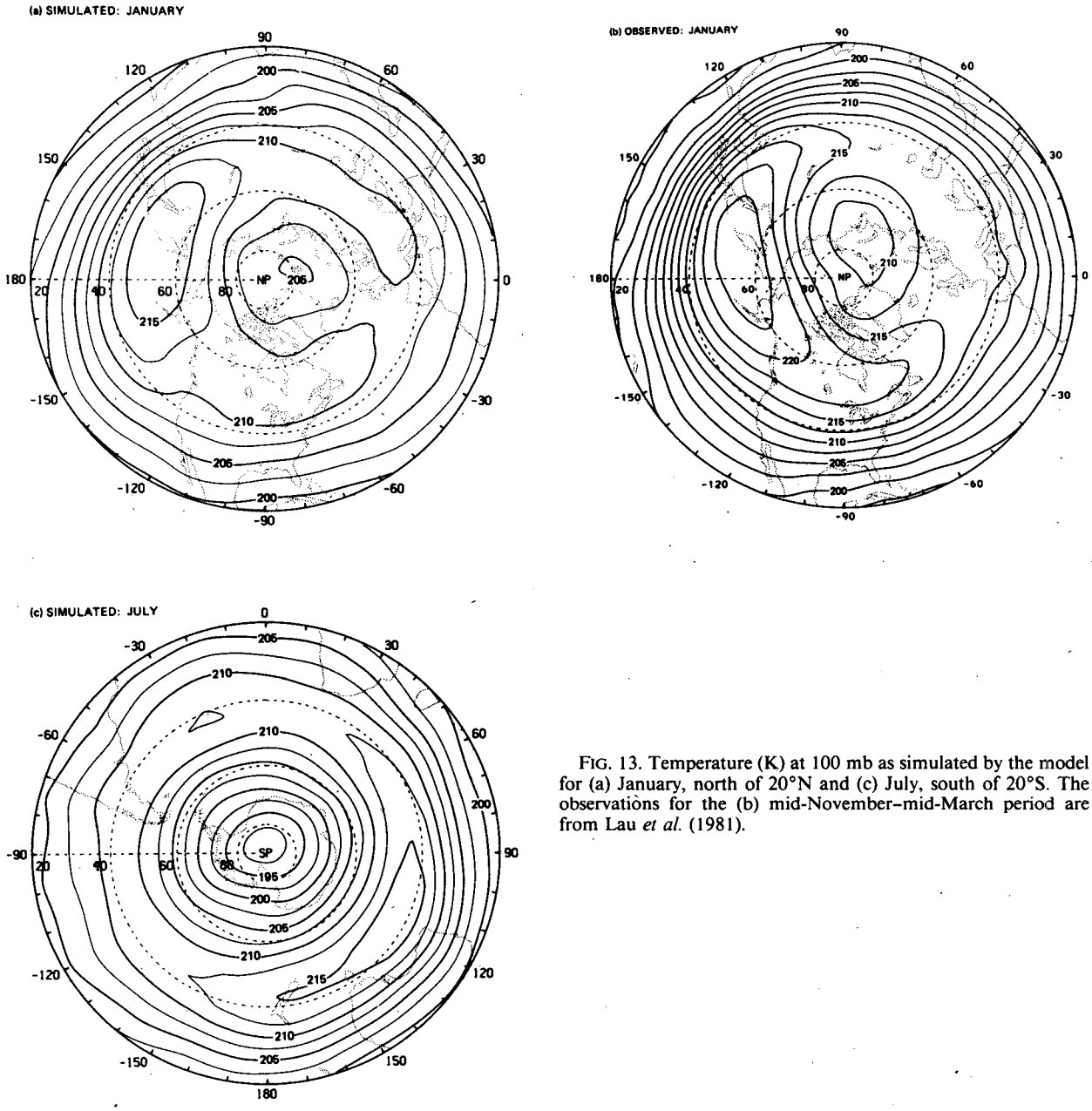

FIG. 13. Temperature (K) at 100 mb as simulated by the model for (a) January, north of 20°N and (c) July, south of 20°S. The observations for the (b) mid-November–mid-March period are from Lau *et al.* (1981).

h. 10 mb temperature and wind

We show the temperature at 10 mb from the model (Fig. 14a) and the atmosphere (Fig. 14b) for Northern Hemisphere January, the observed distribution being taken from Labitzke *et al.* (1972). At this highest model level we see that the structure of the thermal field differs markedly from that in the lower stratosphere (Fig. 13a). In this region of the middle stratosphere the model shows the north–south temperature gradient to be confined essentially poleward of 50°N. The minimum in the thermal field is not found at the pole but displaced along the meridian running through 20°W. Furthermore, over western North America the model positions a trough in the thermal pattern with an extension westward into the Pacific at 35°N, while favoring a thermal ridge over eastern Asia and the Aleutians. All of these features bear a good resemblance to the actual stratosphere.

In Southern Hemisphere July at 10 mb (Fig. 14c) the model's subtropical zone tends to be a few degrees warmer than the simulation in January for the North-

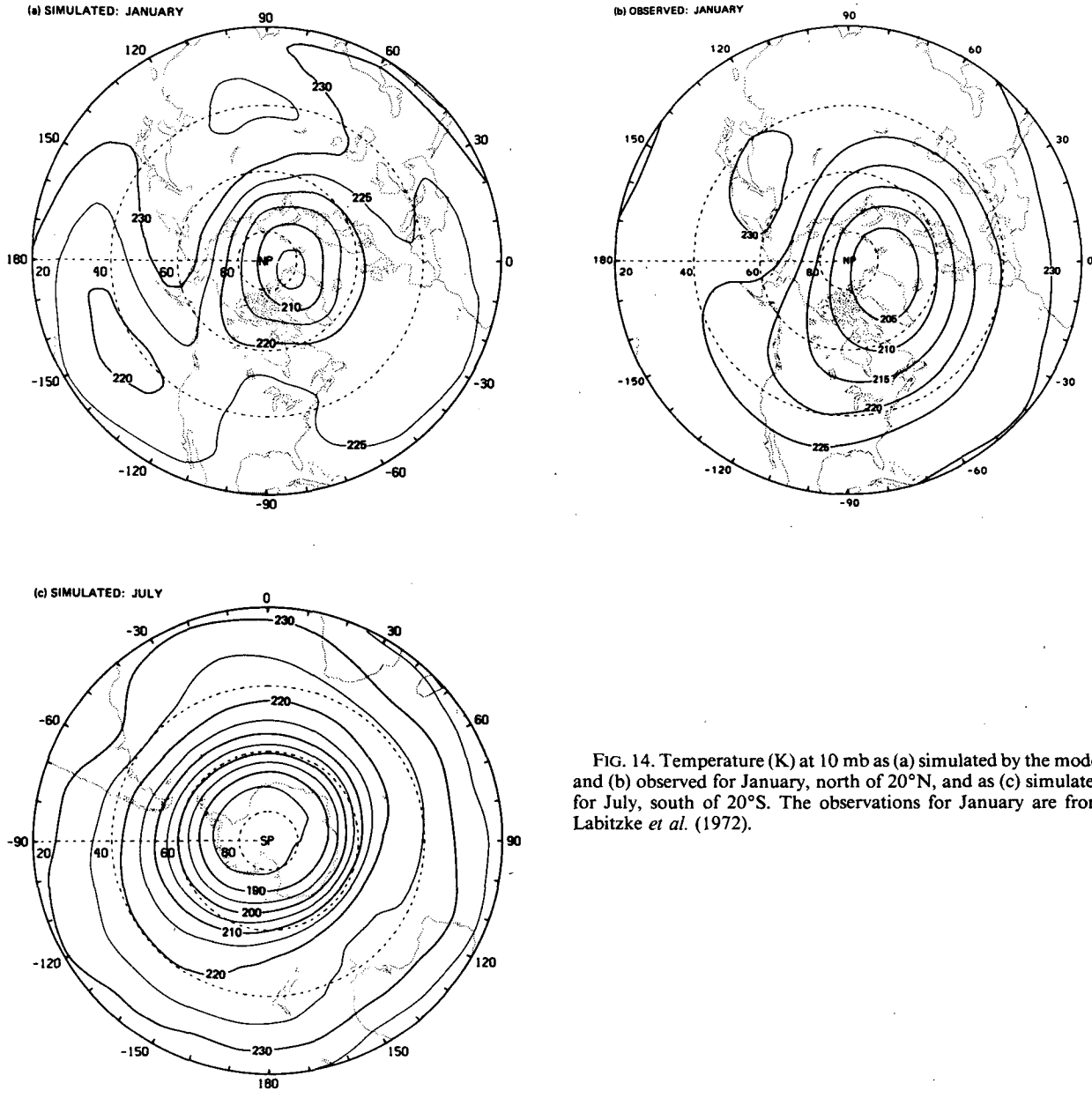

FIG. 14. Temperature (K) at 10 mb as (a) simulated by the model and (b) observed for January, north of 20°N, and as (c) simulated for July, south of 20°S. The observations for January are from Labitzke *et al.* (1972).

ern Hemisphere (Fig. 14a), while the Antarctic temperature minimum is some 20 K lower than the wintertime Arctic value. This is consistent with the more intense zonal wind found in the model stratosphere for Southern Hemisphere July (Fig. 2c).

We compare in Fig. 15 the model's total wind speed at 10 mb with the observed geostrophic wind speed. As indicated by Figs. 14a and 14b the polar vortex in neither the model nor the real atmosphere is centered immediately over the pole. Likewise, the wind-speed minimum shown in Fig. 15a is displaced from 90°N and coincides with the minimum in geopotential height (not shown). The circumpolar jet is 5–10 m s^{-1} weaker than observed, but the configuration is in remarkably good agreement with the observations. We have found that, while the patterns shown in Fig. 15a are relatively constant from one averaging period to the next, the magnitude of the circumpolar jet does vary somewhat, and depends primarily upon the frequency of occurrence of minor stratospheric warmings during the course of the model integration. For example, averaging a later 120-day period shows the jet maximum to exceed the observed values by ~5 m s^{-1}. This suggests that, in

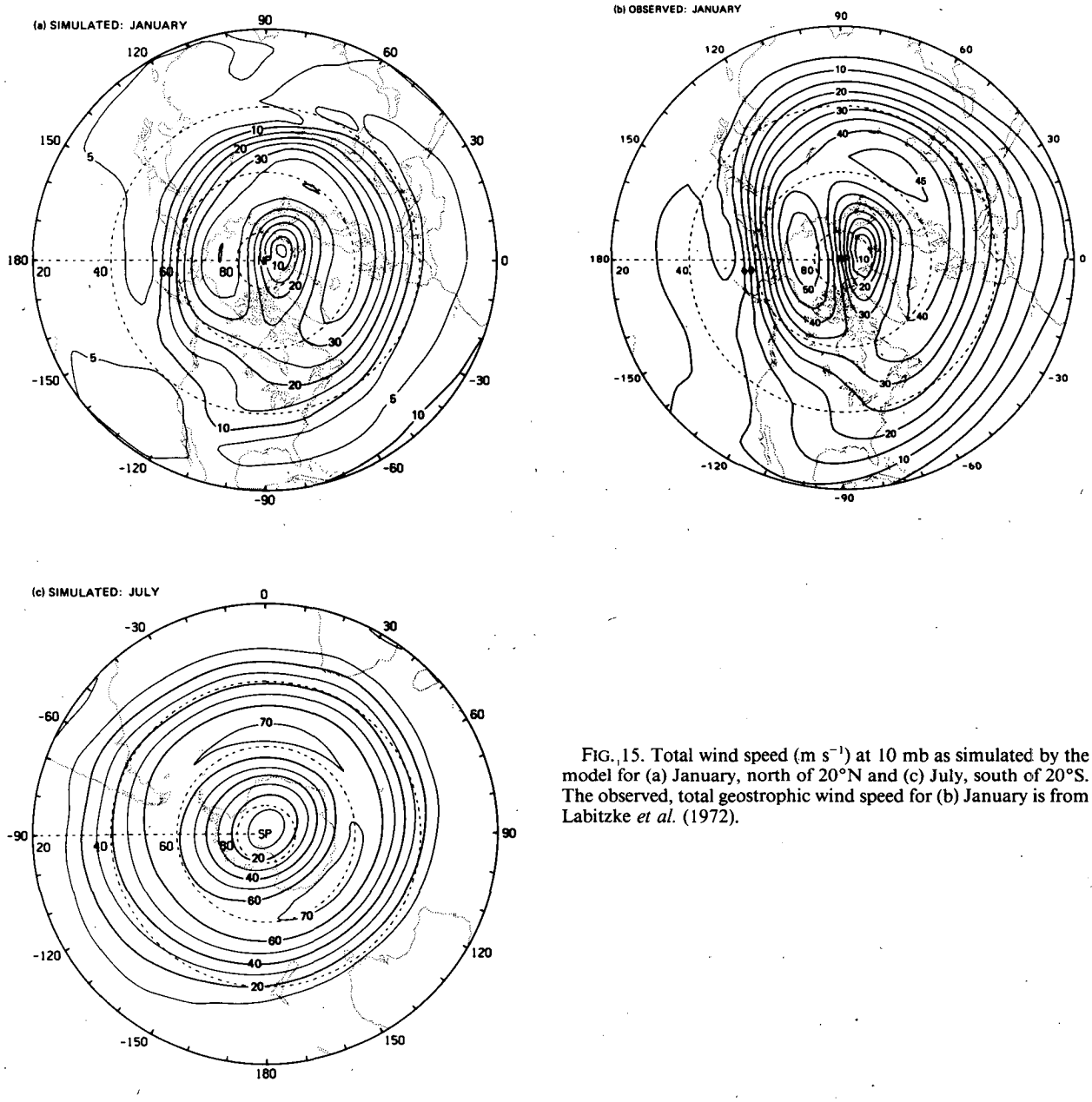

FIG. 15. Total wind speed (m s^{-1}) at 10 mb as simulated by the model for (a) January, north of 20°N and (c) July, south of 20°S. The observed, total geostrophic wind speed for (b) January is from Labitzke *et al.* (1972).

the case of the long-term average, the model is capable of giving a rather good simulation of the Northern Hemisphere stratospheric fields which we have discussed here.

The wind-speed distribution from the model for Southern Hemisphere July is given in Fig. 15c. The circumpolar jet is about twice the strength of its Northern Hemisphere counterpart, and the wind-speed minimum coincides more closely with the pole. Unfortunately, sufficiently detailed observations are not yet available for comparison.

5. Temporal variability

The zonal average of the standard deviation σ of the daily geopotential height z provides a measure of the model's overall temporal variability, i.e.,

$$[\sigma] = [(\overline{z'^2})^{1/2}],$$

where the prime denotes the deviation from a time average, the overbar a 120-day average, and the square brackets denote a zonal average.

In Fig. 16 is shown the latitude–height distribution

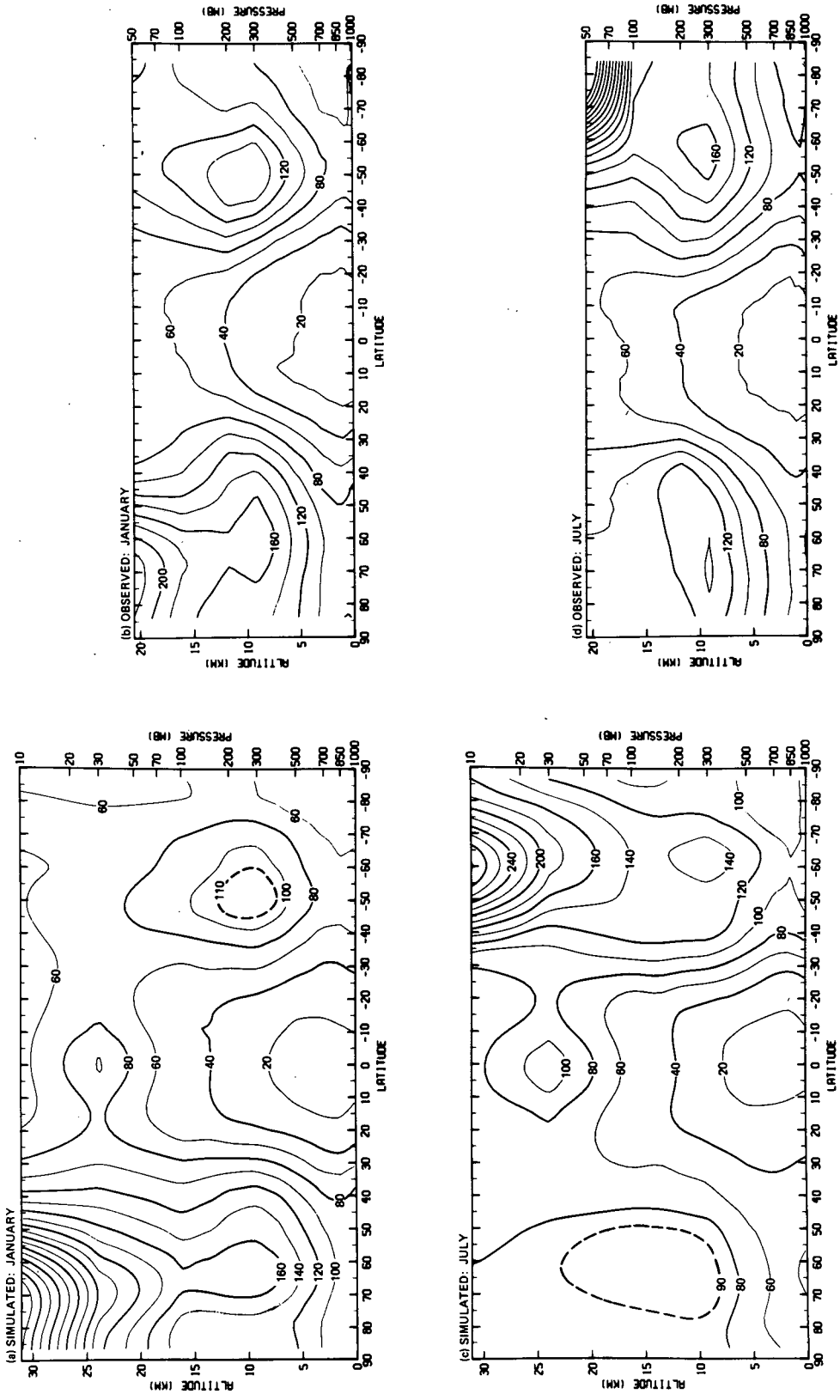

FIG. 16. Zonally averaged standard deviation of daily geopotential height (m) as simulated by the model for (a) January and (c) July. The observations for the (b) December–February and (d) June–August seasons are from Oort (1982).

of [σ] from the model for January and July, together with that observed for the December–February and June–August seasons from Oort (1982).[3] Poleward of 30° in each hemisphere the model variability increases rapidly with latitude in both January and July, while equatorward the model variability is greatly diminished, in general agreement with the atmosphere. The model's variability in the tropics is slightly less than that observed (by ~5 m at 200 mb in January), though it is not as suppressed as that reported by Manabe and Hahn (1981) for the GFDL spectral model. Near the tropopause at 60°N in Northern Hemisphere January, the atmosphere possesses a maximum, which is successfully captured in the model result, while its counterpart for the same month in the Southern Hemisphere is somewhat underestimated.

In the June–August season the observations also show a peak in variability in each hemisphere. The one in the Northern Hemisphere is smaller than, and has shifted some 10° poleward of, its wintertime maximum. The model also shows a maximum in each hemisphere, although the one at 65°N is too weak. The model does capture the increased variability from summer to winter in the Southern Hemisphere, though it underestimates somewhat the atmosphere's variability in this region. In each winter hemisphere, both the observations and the model exhibit substantial variability in the stratosphere at high latitudes.

In summary, the model simulates with considerable success the zonal-mean variability in the daily geopotential height.

6. Summary and conclusions

In this study, we have reported on extended integrations carried out with the spectral general circulation model of Bourke *et al.* (1977), which has undergone further development at the National Center for Atmospheric Research. The model, truncated rhomboidally at wavenumber 15, has been run with both perpetual January and July forcing, and we have examined a limited number of fields averaged over the last 120 days of 200-day runs. Comparison of these model results with observations has permitted the evaluation of the model's capability in simulating these seasonal extremes.

The model is successful in simulating most of the important features of the latitude–height distribution of the zonal wind. In particular, the separation between the tropospheric and stratospheric jets and the moderate wind speeds in the polar–night stratosphere are well captured by the model. We believe the reasons for this success are rooted in the treatment of radiative processes and radiative-dynamical interactions, and this issue is explored in detail by Ramanathan *et al.* (1983).

The major features appearing in the observed surface pressure distribution are also present in the model result with the exception of the model's excessive pressures over subtropical continents in the winter hemisphere, and its deintensification of the thermal lows in January over South America and Africa. This latter deficiency, as well as the lower-than-observed surface air temperature, may, perhaps, be a result of the implicitly assumed constant soil moisture. This conclusion is based upon a sensitivity experiment which we have discussed. Away from the ground we also find the model atmosphere cooler than that observed, and have indicated that part of this may be explained with the inclusion of high-level cirrus with non-black emissivity (Ramanathan *et al.*, 1983). None of the simulations here, however, has been made with this anticipated refinement.

Mid- and upper-tropospheric features are well simulated by the model, apart from the regional distribution of the jet streams in Southern Hemisphere July. The regional distributions of temperature and wind in the model stratosphere compare favorably with that of the actual stratosphere.

The level of temporal variability, as measured by the zonally averaged standard deviation of geopotential-height fluctuations, is comparable to that found in the actual atmosphere. Furthermore, it will be shown in a future paper that the regional distributions of variance generated by the model bear a good resemblance to those observed.

In summary, we find that the current model is capable of yielding a good simulation of the large-scale features of the atmosphere. In its present state the model could be used for the study of the general circulation, or, with refinements in the treatment of surface hydrology, could serve as the atmospheric component in an ocean–atmosphere model for use in climate studies.

Acknowledgments. This study was begun while three of us (EJP, RCM, KP) were Visiting Scientists at NCAR. Dr. C. Leith's interest in and support of this work were instrumental for its completion. We are grateful to Dr. C. Temperton for making his vectorized fast-Fourier transform available to us. Dr. A. Oort provided us with data on atmospheric variability prior to its publication. G. Bates provided programming assistance in the preparation of some of the figures. One of us (EJP) has also received support from the Climate Dynamics Program in the Atmo-

[3] The observations of [σ] were derived by first removing the 3-month seasonal mean from the data for each year. Hence, the observed standard deviations in Fig. 16 include contributions from day-to-day variability as well as month-to-month variability within the same season, but exclude year-to-year variability of the seasonal means. The standard deviation presented by Manabe and Hahn (1981), which was also based on Oort's data, included the contribution of interannual variability.

spheric Sciences Division of the National Science Foundation under Grants ATM-7680604 and ATM-8120319.

APPENDIX

Derivation of Model Topography

The data from which the continental elevations were derived were taken from Smith *et al.* (1966) and consisted of orographic heights averaged over 1° by 1° latitude–longitude squares. The values over the ocean (with negative heights) were set to zero, and then the entire field was smoothed and interpolated to the Gaussian grid. This was done as follows. At each Gaussian gridpoint there was defined a weighting function w, where

$$w = \exp\{-\tfrac{1}{2}[(x/\sigma_x)^2 + (y/\sigma_y)^2]\}. \quad \text{(A1)}$$

In (A1), x and y denote the eastward and northward distances, respectively, from the Gaussian gridpoint, and the half-width of the weighting function is defined by σ_x and σ_y. We have taken $\sigma_x = \sigma_y = aS$ with a the earth's radius and S an angular increment in latitude. Distances may be expressed in terms of longitude λ_i and latitude ϕ_j, so that (A1) may be rewritten as

$$w_{ij} = \exp[-\tfrac{1}{2}S^{-2}(\lambda_i^2 \cos^2\phi + \phi_j^2)], \quad \text{(A2)}$$

where the subscripts denote an indexing of the fine-grid locations (at which the raw data are defined) surrounding the point in question. We then define height H on the Gaussian grid from the expression

$$H = \frac{\sum w_{ij}h_{ij}}{\sum w_{ij}}, \quad \text{(A3)}$$

where h_{ij} is the raw data at 1° by 1° intersections. Each summation refers to a double sum over those points on the fine grid contained within the "influence" region $|\lambda_i| \leqslant 3S$, $|\phi_j| \leqslant 3S$. Once obtained on the Gaussian grid, the continental elevations were spectrally analyzed in the same manner as the other model fields.

We examined the resulting, smoothed topography using a broad range of S. Of the several representations, we selected two, which we termed "rough" and "smooth," for further consideration, based upon the depth of the holes off the coasts of continents with sharp topographic features. By carrying out extended model integrations, we explored to what extent the choice of topography influenced the model simulations. The degree of influence was not great, but certain aspects of the simulations led us to select the "rough" topography ($S = 0.5°$) shown in Fig. 1a as the standard topography. This may be contrasted with the somewhat smoother topography used by McAvaney *et al.* (1978, their Fig. 1a).

REFERENCES

Alexander, R. C., and R. L. Mobley, 1976: Monthly average sea-surface temperatures and ice-pack limits on a 1° global grid. *Mon. Wea. Rev.*, **104,** 143–148.

Blackmon, M. L., 1976: A climatological spectral study of the 500 mb geopotential height of the Northern Hemisphere. *J. Atmos. Sci.*, **33,** 1607–1623.

——, J. M. Wallace, N.-C. Lau and S. L. Mullen, 1977: An observational study of the Northern Hemisphere wintertime circulation. *J. Atmos. Sci.*, **34,** 1040–1053.

Bourke, W., 1974: A multi-level spectral model. I. Formulation and hemispheric integrations. *Mon. Wea. Rev.*, **102,** 687–701.

——, B. McAvaney, K. Puri and R. Thurling, 1977: Global modeling of atmospheric flow by spectral methods. *Methods in Computational Physics,* Vol. 17, *General Circulation Models of the Atmosphere,* J. Chang, Ed., Academic Press, 267–324.

Eliasen, E., B. Machenhauer and E. Rasmussen, 1970: On a numerical method for integration of the hydrodynamical equations with a spectral representation of the horizontal fields. Rep. No. 2, Institute for Theoretical Meteorology, University of Copenhagen, 35 pp. [Available from NCAR Library as Rep. No. 10230].

Ellsaesser, H. W., 1966: Evaluation of spectral versus grid methods of hemispheric numerical weather prediction. *J. Appl. Meteor.*, **5,** 246–262.

Holton, J. R., 1975: *The Dynamic Meteorology of the Stratosphere and Mesosphere. Meteor. Monogr.,* No. 37, Amer. Meteor. Soc., 216 pp.

Labitzke, K., and collaborators, 1972: *Climatology of the Stratosphere in the Northern Hemisphere, Part 1. Heights, Temperatures and Geostrophic Resultant Wind Speeds at 100, 50, 30 and 10 mb. Meteor. Abhandl.,* **100,** No. 4, 286 pp.

Lau, N.-C., 1978: On the three-dimensional structure of the observed transient eddy statistics of the Northern Hemisphere wintertime circulation. *J. Atmos. Sci.*, **35,** 1900–1923.

——, and A. H. Oort, 1981: A comparative study of observed Northern Hemisphere circulation statistics based on GFDL and NMC analyses. Part I: The time-mean fields. *Mon. Wea. Rev.*, **109,** 1380–1403.

——, G. H. White and R. L. Jenne, 1981: Circulation statistics for the extratropical Northern Hemisphere based on NMC analyses. NCAR Tech. Note TN-171+STR, 138 pp.

Manabe, S., and J. D. Mahlman, 1976: Simulation of seasonal and interhemispheric variations in the stratospheric circulation. *J. Atmos. Sci.*, **33,** 2185–2217.

——, and D. G. Hahn, 1981: Simulation of atmospheric variability. *Mon. Wea. Rev.*, **109,** 2260–2286.

——, J. Smagorinsky and R. F. Strickler, 1965: Simulated climatology of a general circulation model with a hydrologic cycle. *Mon. Wea. Rev.*, **93,** 769–798.

——, —— and J. L. Holloway, Jr., 1979: Climate simulations with GFDL spectral models of the atmosphere: Effect of spectral truncation. Report of the JOC Study Conference on Climate models: Performance, Intercomparison and Sensitivity Studies, Washington, DC, 3–7 April 1978. *GARP Publ. Ser.,* No. 22, 41–94 [NTIS N8027917].

McAvaney, B. J., W. Bourke and K. Puri, 1978: A global spectral model for simulation of the general circulation. *J. Atmos. Sci.*, **35,** 1557–1583.

Newell, R. E., J. W. Kidson, D. G. Vincent and G. J. Boer, 1972: *The General Circulation of the Tropical Atmosphere and Interactions with Extratropical Latitudes,* Vol. 1. The MIT Press, 258 pp.

——, ——, —— and ——, 1974: *The General Circulation of the Tropical Atmosphere and Interactions with Extratropical Latitudes,* Vol. 2. The MIT Press, 371 pp.

O'Neill, A., R. L. Newson and R. J. Murgatroyd, 1982: An analysis of the large-scale features of the upper troposphere and the stratosphere in a global, three-dimensional, general circulation model. *Quart. J. Roy. Meteor. Soc.*, **108,** 25–53.

Oort, A. H., 1983: *Global Atmospheric Circulation Statistics, 1958–1973.* NOAA Prof. Paper No. 14, U.S. Government Printing Office, Washington, DC (in press).

Orszag, S. A., 1970: Transform method for the calculation of vector-coupled sums: Application to the spectral form of the vorticity equation. *J. Atmos. Sci.*, **27**, 890–895.

Phillips, N. A., 1957: A coordinate system having some special advantages for numerical forecasting. *J. Meteor.*, **14**, 184–185.

Physick, W. L., 1981: Winter depression tracks and climatological jet streams in the Southern Hemisphere during the FGGE year. *Quart. J. Roy. Meteor. Soc.*, **107**, 883–898.

Ramanathan, V., E. J. Pitcher, R. C. Malone and M. L. Blackmon, 1983. The response of a spectral general circulation model to refinements in radiative processes. *J. Atmos. Sci.*, **40**, 605–630.

Robert, A. J., 1969: Integration of a spectral model of the atmosphere by the implicit method. *Proc. WMO/IUGG Symposium on Numerical Weather Prediction*, Tokyo, Japan Meteor. Agency, pp. VII-19–VII-24 [Available from NCAR Library].

Schutz, C., and W. L. Gates, 1971: Global climatic data for surface, 800 mb, 400 mb: January. Advanced Research Projects Agency, Rep. R-915-ARPA, Rand Corporation, Santa Monica, 173 pp. [NTIS AD-736204].

——, and ——, 1972a: Supplemental global climatic data for surface, 800 mb, 400 mb: January. Advanced Research Projects Agency, Rep. R-915/1-ARPA, Rand Corporation, Santa Monica, 41 pp. [NTIS AD-744633].

——, and ——, 1972b: Global climatic data for surface, 800 mb, 400 mb: July. Advanced Research Projects Agency, Rep. R-1029-ARPA, Rand Corporation, Santa Monica, 180 pp. [NTIS AD-760283].

Smith, S. M., H. W. Menard and G. F. Sharman, 1966: Worldwide ocean depths and continental elevations averaged for areas approximating one degree squares of latitude and longitude. SIO Ref. Rep. 65-8, Scripps Institution of Oceanography, La Jolla, 14 pp. [Available from Data Archive Section, NCAR].

Vincent, D. G., 1968: Mean meridional circulation in the Northern Hemisphere lower stratosphere during 1964 and 1965. *Quart. J. Roy. Meteor. Soc.*, **94**, 333–349.